energies

MDPI

Article

A Discrete Current Controller for High Power-Density Synchronous Machines

Hongtai Ma [1,2], Li Li [2], Yingpeng Fan [1], Youguang Guo [2], Zhihui Jin [1] and Jian Luo [1,*]

[1] Shanghai Key Laboratory of Power Station Automation Technology, School of Mechatronics Engineering and Automation, Shanghai University, Shanghai 200072, China
[2] School of Electrical and Data Engineering, University of Technology Sydney, Ultimo, NSW 2007, Australia
* Correspondence: luojian@shu.edu.cn

Abstract: This paper proposes a complex vector discrete current controller based on the flux-linkage data to solve the current loop oscillation problem of high power-density synchronous machines. An offline flux-linkage table measurement method considering cross saturation is introduced, and the data are used to deduce the symmetrical complex vector model. The influence of latch and delay of inverters on the line voltage of machines at high speed is analyzed and compensated during the controller design process. The proposed controller, which only needs to tune one parameter, can deal with the inductance mismatch issues caused by iron core saturation. The controller can be adopted in the current loop of saturated salient or nonsalient synchronous machines. Simulations and experiments have verified the effectiveness of the proposed method.

Keywords: synchronous machines; power density; digital current control; saturation

Citation: Ma, H.; Li, L.; Fan, Y.; Guo, Y.; Jin, Z.; Luo, J. A Discrete Current Controller for High Power-Density Synchronous Machines. *Energies* **2022**, *15*, 6396. https://doi.org/10.3390/en15176396

Academic Editor: Mario Marchesoni

Received: 4 August 2022
Accepted: 30 August 2022
Published: 1 September 2022

Publisher's Note: MDPI stays neutral with regard to jurisdictional claims in published maps and institutional affiliations.

Copyright: © 2022 by the authors. Licensee MDPI, Basel, Switzerland. This article is an open access article distributed under the terms and conditions of the Creative Commons Attribution (CC BY) license (https://creativecommons.org/licenses/by/4.0/).

1. Introduction

Synchronous machines such as salient-pole permanent magnet synchronous machines are widely used in powertrain systems of electric vehicles, aircrafts, and bionic robots for the merits of high power density and high efficiency. In these compact and lightweight scenarios, motor control systems should be able to work at high-speed and peak-torque operating modes shortly to provide higher output power.

As for the high-speed operating mode, current loop performance deteriorates with the speed increase due to the computation and modulation delay. In order to improve stability of the current loop controller at the high speed, the time-lag issue can be addressed by improving the switching frequency and sampling frequency. Compared to synchronous single current sampling and single pulse width modulate duty ratio update (SSSU) control mode, synchronous dual current sampling and dual pulse width modulate duty ratio update (DSDU) is able to double the sampling frequency without increasing the switching frequency [1].

Essentially, switching frequency and sampling frequency are limited by switching loss and computing resources. Modeling the sampling-updating time lag so as to develop a more accurate controller is another solution [2,3]. Predictive control systems such as deadbeat control and finite control set model can also deal with the high-speed operation mode [4–6].

At the same time, the dq-frame machine model introduces the cross-coupling term, which deteriorates the control performance. Incomplete decoupling can cause current ringing and even instability, especially in high-speed regions. There are feedforward decoupling, feedback decoupling, and complex vector decoupling, which achieve a better effect [7]. Taking saturation into consideration, all of these decoupling methods depend on precise *d-q* flux parameters.

However, in peak-torque mode, the current is several times of the rated value, resulting in the parameter change. When motors work beyond the knee point, the saturation of iron cores will lead to severe inductance reduction [8]. Additionally, stator resistance and permanent magnet flux vary with temperature. These parameter mismatches will influence the stability and fast response of the current loop.

Many modern or intelligence control methods are capable of dealing with time-varying and nonlinear problems caused by saturation. For example, adaptive control, sliding mode control, fuzzy control, and artificial neural network control work well without requiring the exact model parameters. Since the 1960s, adaptive control has been well developed. By adaptive law, which can be proved Lyapunov stable, the parameter in the controller is tuned in real time. It can deal with feedback error and parameter change, but the computation is extensive, and the convergence rate cannot be guaranteed. Hence, it is not suitable for the rapidly changing current loop [9,10]. Fuzzy control uses fuzzy logic and experts' experience rather than specific parameters and a detailed model. It realizes robust controllers in certain nonlinear circumstances. However, it relies too much on engineers' experience, which may be inaccurate [11]. The widely used sliding mode control changes the control loop structure to make the error signal converge to zero. It does not require specific model parameters and can achieve high robustness and good dynamic. However, the current chattering in steady state is severe [12,13].

There are also some control methods based on machine parameters. A unifying review of the internal model control (IMC) type schemes was published by Garcia and Morari first in 1982. The IMC principle uses the inverse of the plant model and a low-pass filter to design the controller. The only tuning parameter is the filter bandwidth, making the control system easy to design. When the inductance and resistance are known, the response follows the instruction, and the system can be regarded as an open-loop control system. Nevertheless, the response will deteriorate when the inductance and resistance are inaccurate. It may even result in divergence when the magnetic circuit is highly saturated [14,15]. IMC can also be applied to nonlinear and time-variant systems. However, it involves seeking analytically the inverse of those plants' model, and it contains higher-order derivatives and is therefore sensitive to noise and numerical errors. Hence, it cannot provide a satisfactory outcome [16].

In engineering practice, piecewise linearization is frequently adopted. The IMC controller parameters depend on the current interval partitioned for linearization. However, there is no theoretical support on how to choose the partition, and it is difficult to guarantee the system stability. Essentially, IMC is based on the accurate model and appropriate parameters [17].

The concept of complex vector control was proposed by Waldo V. Lyon in 1954. It was regarded as a coordinate transformation initially. The successive scholars expanded it to model nonsalient machines, which simplify voltage equations [18]. The complex vector model transfers the multiple input multiple output (MIMO) system into a single input single output (SISO) system, with which the classical analytical tools of root locus and frequency response can be applied [19].

As for machines with salient poles such as synchronous reluctance motor (SRM) and interior permanent magnet (IPM) synchronous motor, they can be modeled using flux vector state variables to replace the current vector ones due to their naturally symmetric characteristic. This modeling method can achieve good control performance even for high saliency machines [20,21].

The complex vector model based on flux is adopted in this article. Delay and latch in the *d*-*q* synchronous rotating frame system are also analyzed in detail. A discrete controller is proposed for saturated synchronous machines working at high speed. Section 2 establishes an accurate plant model, including the model of synchronous machines with cross-coupling saturation, the nonlinear inductance identification, and the output voltage error caused by the delay of the discrete system. Section 3 gives the design procedures and simulation results of classical PI controller based on the IMC and flux-linkage vector-

based model. Section 4 presents the experimental setup and results. The simulation and experimental results verify the effectiveness of the proposed controller, which can improve the control performance of synchronous machines outputting peak power. Finally, Section 5 concludes this article.

2. System Modeling

2.1. Model of Salient Machines

The voltage equation of salient machines in the *d-q* synchronous rotating frame can be described as follows:

$$\begin{bmatrix} u_d \\ u_q \end{bmatrix} = R\begin{bmatrix} i_d \\ i_q \end{bmatrix} + \frac{d}{dt}\begin{bmatrix} \psi_d\left(i_d, i_q\right) \\ \psi_q\left(i_d, i_q\right) \end{bmatrix} + \omega_e \begin{bmatrix} -\psi_q\left(i_d, i_q\right) \\ \psi_d\left(i_d, i_q\right) + \lambda_{pm}\left(i_d, i_q\right) \end{bmatrix} \tag{1}$$

where u_d and u_q are the stator voltages of direct and quadrature axes, i_d and i_q are stator currents of direct and quadrature axis, R is stator winding resistance, and ω_e is the electrical rotational speed. ψ_d and ψ_q are the flux linkages of direct and quadrature axes due to the stator current excitation. Due to the magnetic coupling in direct and quadrature axes, ψ_d is not only influenced by i_d, but also i_q, and so is ψ_q. For IPM machines, λ_{pm} represents permanent magnet flux linkage, which depends on stator currents. As for SRM, λ_{pm} is equal to zero.

$$\begin{bmatrix} u_d \\ u_q \end{bmatrix} = R\begin{bmatrix} i_d \\ i_q \end{bmatrix} + \begin{bmatrix} L_{dd}\left(i_d, i_q\right) & L_{dq}\left(i_d, i_q\right) \\ L_{qd}\left(i_d, i_q\right) & L_{qq}\left(i_d, i_q\right) \end{bmatrix} \frac{d}{dt}\begin{bmatrix} i_d \\ i_q \end{bmatrix} + \omega_e \begin{bmatrix} -L_q\left(i_d, i_q\right) i_q \\ L_d\left(i_d, i_q\right) i_d + \lambda_{pm}\left(i_d, i_q\right) \end{bmatrix} \tag{2}$$

By defining (3)–(5), Equation (2) can be derived from (1), where $L_{dd}, L_{dq}, L_{qd}, L_{qq}$ are dynamic inductance; L_d, L_q are static inductance.

$$L_{dd}\left(i_d, i_q\right) = \frac{\partial \psi_d\left(i_d, i_q\right)}{\partial i_d}, L_{dq}\left(i_d, i_q\right) = \frac{\partial \psi_d\left(i_d, i_q\right)}{\partial i_q} \tag{3}$$

$$L_{qd}\left(i_d, i_q\right) = \frac{\partial \psi_q\left(i_d, i_q\right)}{\partial i_d}, L_{qq}\left(i_d, i_q\right) = \frac{\partial \psi_q\left(i_d, i_q\right)}{\partial i_q} \tag{4}$$

$$L_d\left(i_d, i_q\right) = \frac{\psi_d\left(i_d, i_q\right)}{i_d}, L_q\left(i_d, i_q\right) = \frac{\psi_q\left(i_d, i_q\right)}{i_q} \tag{5}$$

The plant described by (2) cannot be handled with the classical control theory for its nonlinearity. When the saturation and cross saturation effect are negligible, all the dynamic and static inductance in (5) can be treated as constants, as shown in (6).

$$\begin{aligned} &\lambda_{pm}\left(i_d, i_q\right) = \lambda_{pm} \\ &L_{dd}\left(i_d, i_q\right) = L_d\left(i_d, i_q\right) = L_d \\ &L_{qq}\left(i_d, i_q\right) = L_q\left(i_d, i_q\right) = L_q \\ &L_{qd}\left(i_d, i_q\right) = L_{dq}\left(i_d, i_q\right) = 0 \end{aligned} \tag{6}$$

$$\begin{bmatrix} u_d \\ u_q \end{bmatrix} = R\begin{bmatrix} i_d \\ i_q \end{bmatrix} + \begin{bmatrix} L_d & 0 \\ 0 & L_q \end{bmatrix} \frac{d}{dt}\begin{bmatrix} i_d \\ i_q \end{bmatrix} + \omega_e \begin{bmatrix} -L_q i_q \\ L_d i_d + \lambda_{pm} \end{bmatrix} \tag{7}$$

Equation (7) can be transformed into two SISO systems after decoupling. The parameters identification of the system is presented in the next part.

2.2. Flux-Linkage Identification of Saturated Machines

When machines are intensely saturated, Equations (1)–(2) are more accurate than (6)–(7). The parameters in (1)–(2) can be identified by several methods [22,23]. They can be categorized as online and offline identification in terms of the working process, or as locked rotor or rotating rotor in terms of the test condition. This article concerns the flux linkage variation caused by current excitation rather than other variables such as temperature; thus, the parameters are measured at 25 °C (with a TOH-408JXS constant temperature chamber of TOMILO). The interference term $\omega_e\left[-\psi_q\left(i_d,i_q\right)\ \ \psi_d\left(i_d,i_q\right)+\lambda_{pm}\left(i_d,i_q\right)\right]^T$ in (1) is equal to zero if the rotor is locked with a magnetic particle brake, which deduces (8)–(10).

$$\begin{bmatrix} u_d \\ u_q \end{bmatrix} = R\begin{bmatrix} i_d \\ i_q \end{bmatrix} + \frac{d}{dt}\begin{bmatrix} \psi_d\left(i_d,i_q\right) \\ \psi_q\left(i_d,i_q\right) \end{bmatrix} \tag{8}$$

$$\psi_d\left(i_d(t),i_q(t)\right) = \int_o^t \left[u_d(\tau) - Ri_d(\tau)\right]d\tau \tag{9}$$

$$\psi_q\left(i_d(t),i_q(t)\right) = \int_o^t \left[u_q(\tau) - Ri_q(\tau)\right]d\tau \tag{10}$$

The inverter is controlled in current closed-loop mode or open-loop voltage output mode to acquire the flux linkage including the cross-coupling saturation. Taking $\psi_d\left(i_d,i_q\right)$ identification as an example, a current loop is used to make $i_q(t)=i_{q0}$, while voltage u_d is changing in a stepwise manner, namely $u_d(t)=\pm u_{d0}$. The voltage u_{d0} must be high enough so that the response current i_d covers the complete operating range.

The waveforms of $i_d(t)$ and $u_d(t)$ are recorded to calculate $\psi_d\left(i_d(t),i_{q0}\right)$ in (11). The resistance R can be worked out with the voltage and steady-state current.

$$\psi_d\left(i_d(t),i_{q0}\right) = \int_0^t \left[u_d(\tau) - Ri_d(\tau)\right]d\tau\Big|_{i_q(t)=i_{q0}} \tag{11}$$

By repeating the aforementioned procedures and changing $i_q = i_{q1}, i_{q2}\cdots$, the relationship between ψ_d and $\left(i_d,i_q\right)$ can be derived, as shown in Figure 1.

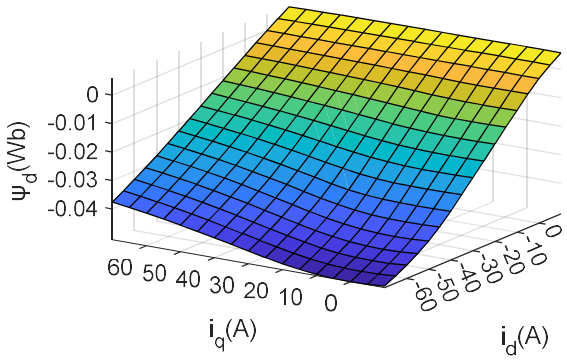

Figure 1. Measurement result of direct-axis flux linkage due to current excitation.

By using the same way and (12), ψ_q can also be calculated. Different from ψ_d, applying $\pm u_{q0}$ will lead to drastic changes in the output torque. The machine's fixing should then be strengthened as much as possible, and backlashes should be taken care of to avoid rotor position variation and then to increase the identification accuracy.

$$\psi_q\left(i_{d0}, i_q(t)\right) = \int_0^t \left[u_q(\tau) - R i_q(\tau)\right] d\tau \Big|_{i_d(t)=i_{d0}} \tag{12}$$

With the flux-linkage data in Figures 1 and 2, the look-up tables of $L_{dd}\left(i_d, i_q\right), L_{dq}\left(i_d, i_q\right), L_{qd}\left(i_d, i_q\right), L_{qq}\left(i_d, i_q\right), L_d\left(i_d, i_q\right), L_q\left(i_d, i_q\right), \lambda_{pm}\left(i_d, i_q\right)$ can be computed by (3)–(5). With these data and (2), the model of saturated PMSM can be established [24].

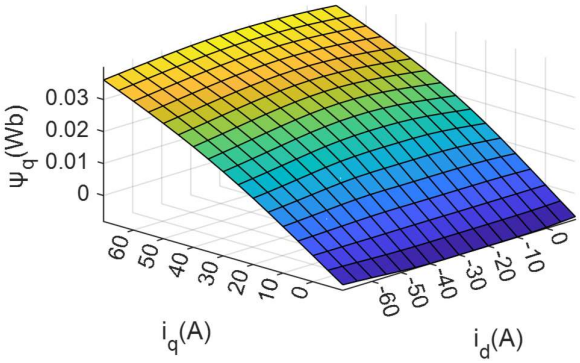

Figure 2. Measurement result of quadrature axis flux linkage.

2.3. The Effect of Latch and Delay in Inverters

With the development of digital control, DSP and insulated gate bipolar transistor (IGBT) have been widely used in the machine control area. The current is sampled, transformed, and input into the current loop to calculate the voltage command value. Then, the converter outputs the voltage after a short delay, which is relative to the sampling period. If the machine is working in high-speed mode, the delay of the sampling–updating–outputting procedure cannot be neglected. Compared to synchronous SSSU, synchronous DSDU can double the sampling frequency and halve the delay time without increasing the switching loss.

As shown in Figure 3, sampling is synchronous with carrier waves. In DSDU, sampling occurs at the peak and valley value of carrier waves, and updating occurs after sampling. For example, the DSP samples at t_1 and updates at t_2. The ordinary seven-segments voltage vector is divided into two four-segment voltage vectors, namely $\overrightarrow{u_{dq}}(k-2)$ of $t_1 - t_2$ and $\overrightarrow{u_{dq}}(k-1)$ of $t_2 - t_4$. It can be approximately regarded that the average value of $\overrightarrow{u_{dq}}(k-1)$ occurs at the midpoint of t_2 and t_4, namely t_3. The voltage vector command value corresponding to sample time t_1 is not applied to the winding until the t_3 moment. The delay between sampling and outputting is equal to $\frac{3T_s}{2}$.

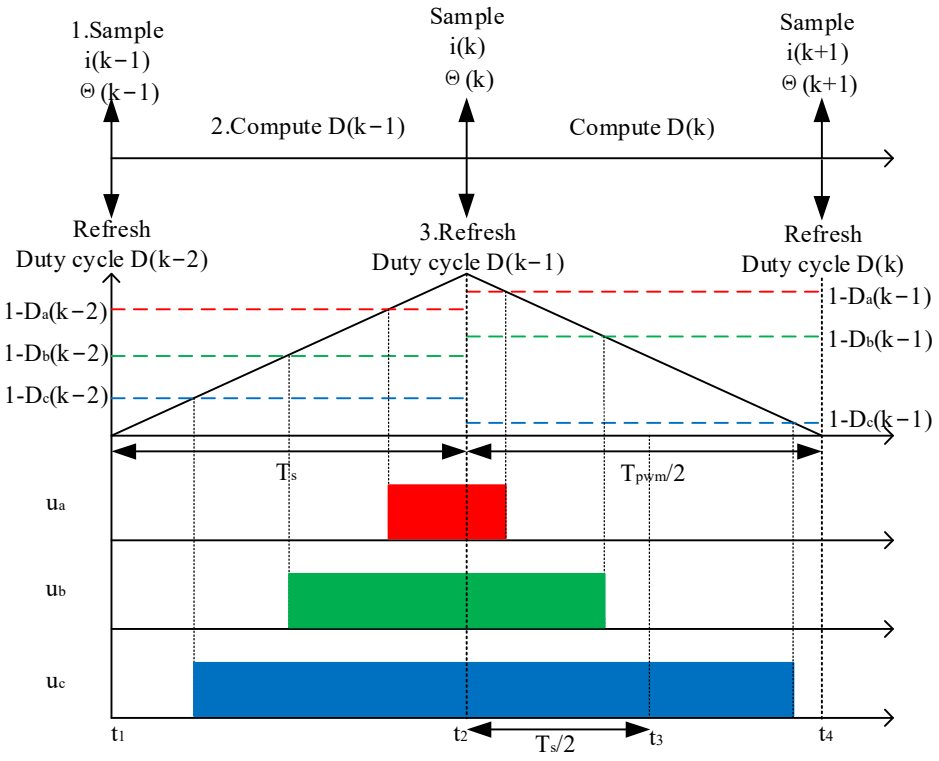

Figure 3. Chronological chart of sampling and outputting of DSDU.

To illustrate the deviation between the given value and the output value, Figure 4 presents a two-pole machine model with the rotor rotating (aligned with direct-axis). Supposing the rotor speed ω_e is steady, the rotor position of the north pole at the three sampling instants t_1, t_2 and t_4 are $\mathrm{d}(t_1)$, $\mathrm{d}(t_2)$, $\mathrm{d}(t_4)$. After sampling at t_1 and computing during $t_1 - t_2$, the duty cycle information is updated to the register at t_2. During the outputting time ($t_2 - t_4$), the rotor still rotates at the speed of ω_e. The actual output voltage vector during $t_2 - t_4$ can be calculated by (13),

$$\overrightarrow{u_{dq}}(t) = \overrightarrow{u_{dq}^{*}}(k) e^{j\theta(k)} e^{-j\theta(k) - j\omega_e t} \qquad ,t \in [t_2, t_4] \tag{13}$$

where $e^{-j\theta(k)-j\omega_e t}$ and $e^{j\theta(k)}$ denote Park's transformation factor and inverse Park's transformation factor. $\overrightarrow{u_{dq}^{*}}(k)$ denotes the voltage command value. The average output voltage is given in (14).

$$\overrightarrow{u_{dq}}(k+1) = \frac{1}{T_s}\int_{T_s}^{2T_s} \overrightarrow{u_{dq}}(t)d\tau = \frac{\frac{1}{2}\omega_e T_s}{\mathrm{Sin}\left(\frac{\omega_e T_s}{2}\right)} \overrightarrow{u^{*}}(k) e^{-j\frac{3}{2}\omega_e T_s} \tag{14}$$

Equation (14) shows that the magnitude error is $\omega_e T_s / \left(2\mathrm{Sin}\left(\omega_e T_s/2\right)\right)$, and the direction error is $e^{-j3\omega_e T_s/2}$. With the increasing ω_e, the errors become non-ignorable. The errors should be compensated in the control system.

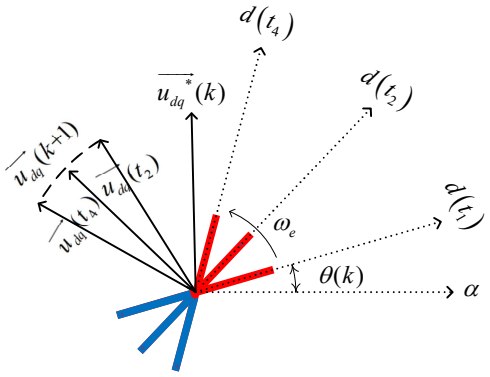

Figure 4. Voltage complex vector plot of a rotating PMSM.

3. Controller Design and Simulation

3.1. PI Controllers Based on IMC Principles

A decoupled PI controller based on the internal model principle is the most widely used solution for its simple structure and good performance. In this section, a brief introduction of the controller is given. For diagonal IMC (DIMC), decoupling should be implemented first to remove the cross-coupling of direct and quadrature axis terms in (7). Equation (15) represents two separate SISO systems, where $u_d^{'}$ and $u_q^{'}$ are direct and quadrature axes voltages after decoupling. To achieve a good dynamic performance, the voltage drop caused by crossover inductance and permanent flux linkage $\omega_e\left[-L_q i_q \quad L_d i_d + \lambda_{pm}\right]^T$ should be added back to $\left[u_d^{'}(s) \quad u_q^{'}(s)\right]^T$ during realization.

$$\begin{aligned}\begin{bmatrix} u_d^{'} \\ u_q^{'} \end{bmatrix} &= \begin{bmatrix} u_d \\ u_q \end{bmatrix} - \omega_e \begin{bmatrix} -L_q i_q \\ L_d i_d + \lambda_{pm} \end{bmatrix} \\ &= R\begin{bmatrix} i_d \\ i_q \end{bmatrix} + \begin{bmatrix} L_d & 0 \\ 0 & L_q \end{bmatrix} \frac{d}{dt} \begin{bmatrix} i_d \\ i_q \end{bmatrix}\end{aligned} \tag{15}$$

Equation (16) can be obtained from (15) in the frequency domain, where s denotes the Laplace factor.

$$\begin{bmatrix} i_d \\ i_q \end{bmatrix} = G_{Plant}(s) * \begin{bmatrix} u_d^{'}(s) \\ u_q^{'}(s) \end{bmatrix} = \begin{bmatrix} \frac{1}{R + sL_d} & 0 \\ 0 & \frac{1}{R + sL_q} \end{bmatrix} \begin{bmatrix} u_d^{'}(s) \\ u_q^{'}(s) \end{bmatrix} \tag{16}$$

According to the DIMC principle, the current controller can be designed as (17), where $K_d = \alpha L_d$, $K_q = \alpha L_q$, $T_{id} = \frac{L_d}{R}$, $T_{iq} = \frac{L_q}{R}$ and α is the pending parameter [25].

$$C(s) = \begin{bmatrix} K_d\left(1 + \frac{1}{sT_{id}}\right) & 0 \\ 0 & K_q\left(1 + \frac{1}{sT_{iq}}\right) \end{bmatrix} \tag{17}$$

The closed-loop transfer function $G_{dPI}(s)$ is a first-order lag as shown in (18). The expecting bandwidth is determined by the only unknown parameter α.

$$G_{clPI}(s)=\frac{C(s)G_{Plant}(s)}{1+C(s)G_{Plant}(s)}=\begin{bmatrix}\frac{\alpha}{s+\alpha} & 0\\ 0 & \frac{\alpha}{s+\alpha}\end{bmatrix} \tag{18}$$

Because Laplace transformation is only applicable to the linear time-invariant system, theoretically speaking, the parameters in (17) should be fixed in the control period. When saturation occurs, the inductance and thus the stability margin will decrease, leading to the overshoot and even oscillation of the current. The delay of the control system is also neglected, and therefore, the expected bandwidth α cannot be achieved. The controller proposed below which is based on the flux-linkage state and data can handle these issues.

3.2. Controller Based on Flux-Linkage Data

Define intermediate voltage v_d and v_q as shown in (19). Deduced from (1), Equation (20) describes the relationship between voltage and flux linkage.

$$\begin{bmatrix}v_d\\ v_q\end{bmatrix}=\begin{bmatrix}u_d\\ u_q\end{bmatrix}-R\begin{bmatrix}i_d\\ i_q\end{bmatrix}-\omega_e\begin{bmatrix}0\\ \lambda_{pm}(i_d,i_q)\end{bmatrix} \tag{19}$$

$$\frac{d}{dt}\begin{bmatrix}\psi_d(i_d,i_q)\\ \psi_q(i_d,i_q)\end{bmatrix}=\begin{bmatrix}0 & \omega_e\\ -\omega_e & 0\end{bmatrix}\begin{bmatrix}\psi_d(i_d,i_q)\\ \psi_q(i_d,i_q)\end{bmatrix}+\begin{bmatrix}v_d\\ v_q\end{bmatrix} \tag{20}$$

The complex vector form of (20) is shown in (21), where $\vec{\psi}(i_d,i_q)=\begin{bmatrix}\psi_d(i_d,i_q) & \psi_q(i_d,i_q)\end{bmatrix}^T$, and $\vec{v}=\begin{bmatrix}v_d & v_q\end{bmatrix}^T$. The mechanical time constant is much bigger than the electrical time constant, and the variation of ω_e can be neglected. Equation (21) is a state-space representation that describes a SISO linear time-invariant system.

$$\frac{d\vec{\psi}(i_d,i_q)}{dt}=-\mathrm{j}\omega_e\vec{\psi}(i_d,i_q)+\vec{v} \tag{21}$$

The discrete-time solution of (21) is shown in (22). With the delay in (14) considered, the transfer function of the plant $G_{Plant}(z)$ can be written as (23).

$$\vec{\psi}(k+1)\Big|_{i_d,i_q}=e^{-j\omega_eT_s}\vec{\psi}(k)\Big|_{i_d,i_q}+\frac{1}{j\omega_e}(1-e^{-j\omega_eT_s})\vec{v}(k) \tag{22}$$

$$G_{Plant}(z)=\frac{\vec{\psi}(z)\big|_{i_d,i_q}}{\vec{v}^*(z)}=\frac{1}{j\omega_e z}\frac{1-e^{-j\omega_eT_s}}{ze^{j\frac{3}{2}\omega_eT_s}-e^{j\frac{1}{2}\omega_eT_s}}\frac{\frac{1}{2}\omega_eT_s}{\mathrm{Sin}\left(\frac{1}{2}\omega_eT_s\right)} \tag{23}$$

Based on the accurate discrete model, the controller $G_c(z)$ in (24) can be obtained without discretization procedure. As shown in (25), the closed-loop transfer function $G_{clCV}(z)$ is of simple structure

$$G_c(z)=\frac{k(e^{j\omega_eT_s}-1)}{T_s\left(e^{-j\omega_eT_s}-1\right)}\frac{ze^{j\omega_eT_s}-1}{1-z} \tag{24}$$

$$G_{clCV}(z)=\frac{G_c(z)G_{Plant}(z)}{1+G_c(z)G_{Plant}(z)}=\frac{k}{z^2-z+k} \tag{25}$$

Figure 5 presents the structure of the proposed controller. First, the feedback current (i_d, i_q) is given to the look-up table $\psi_d(i_d, i_q)$ and $\psi_q(i_d, i_q)$ to acquire $\vec{\psi}$. The intermediate voltage $\vec{v}^*$ can be acquired from $\vec{\psi}$. Then, the voltage drop across the resistor and back EMF are added, and the voltage reference value $\vec{u}^*$ is given to the inverter. The complex form has to be transformed into the scalar form using the Euler equation to be implemented in DSP. The sine and cosine values can be calculated and saved into RAM during DSP initialization to increase the code execution efficiency. The flux-linkage table should be large enough to cover the whole dynamic process of the current.

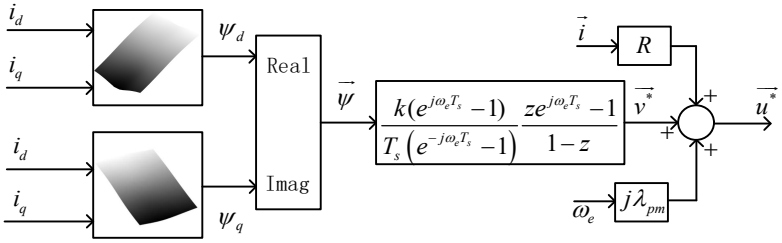

Figure 5. Structure of complex vector current controller based on the flux-linkage data.

3.3. Simulation

The simulation of the PI control and complex vector control is carried out in Matlab/Simulink. The discrete-time step is set as 1 μs, and the switching frequency is set as 10 kHz. The motor module is based on (2) and the inductance table [26]. Voltage controlled voltage source (VCVS) with 1 μs delay is adopted to represent the three-phase full-bridge voltage source inverter (VSI). The complex vector controller $G_c(z)$ multiplied with $0.5\omega_e T_s / \mathrm{Sin}(0.5\omega_e T_s) e^{-j\frac{1}{2}\omega_e T_s}$ is used to compensate for the time delay between VCVS and VSI.

The step response of the closed-loop transfer function of the complex vector controller $G_{clCV}(z)$ with $k = 0.15, 0.3, 0.45$ is simulated, and the results are presented in Figure 6. According to the simulation result, k is set to 0.3 in the following. The c3 dB bandwidth of the closed-loop transfer function $G_{clCV}(z)$ is $12,947\mathrm{rad/s}$ when the sampling frequency is 20 kHz. The −3 dB bandwidth of $G_{clCV}(z)$ is $6473\mathrm{rad/s}$ when the sampling frequency is 10 kHz.

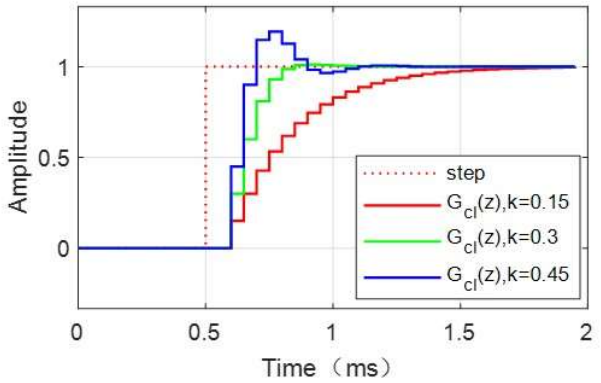

Figure 6. Step response of ideal closed-loop transfer function with different parameters.

As shown in Figure 7, the Bode diagram of the PI control and complex vector control system has the same −3 dB -bandwidth at $\alpha = 12,947 \text{rad}/s$ and $k = 0.3$. However, considering the time-lag effect, the bandwidth of the PI controller is limited. In engineering practice, bandwidth is usually set as $\alpha = 0.5/T_{dealy}$. Since $T_{dealy} = 75\mu s$ in DSDU, the parameter α should be 6667rad/s. Large currents are assigned to the winding to generate short-time peak torques; thus, the motor in this research can be highly saturated, which means that a smaller α is more suitable. The simulation of the two controllers in different working conditions is shown in the following.

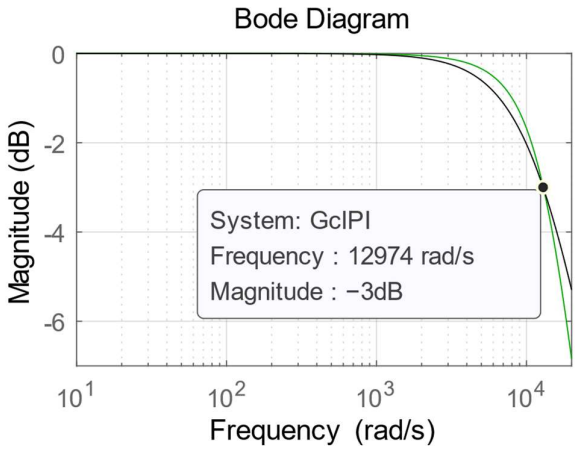

Figure 7. Bode diagram of closed-loop transfer functions (Green line, complex vector controller; Black line, PI controller).

3.3.1. Simulation of the Locked Saturated Machine

To verify the effectiveness of high-current control, the speed is set close to 0 rpm, and the sampling frequency is 20 kHz. According to the simulation and experiment, the control parameters are set as follows, $\alpha = 4000 \text{rad/s}$, $k = 0.3$. In practice, for a saturated salient machine, the dq axes current command trajectories are given through a look-up table to achieve maximum torque per ampere (MTPA) control performance. In this research, the MTPA look-up table is not experimentally calibrated, and the direct axis command current is set as −0.2 times the quadrature one. The quadrature axis current is given an incremental increase of 15 A each 5 ms from 0 to 60 A. The direct axis current is given a decrease step of 3 A each 5 ms from 0 to −12 A

As the simulation results shown in Figures 8 and 9, the current oscillation appears when using the PI controller to deal with the saturated machine. "SR" is the abbreviation of step response in this paper. With the increasing severity of the saturation, the deviation between the current trajectory and step response of the closed-loop transfer function $G_{clPI}(s)$ increases. As for the complex vector controller, the current always follows the step response of the closed-loop transfer function $G_{clCV}(z)$, no matter how saturated the motor is.

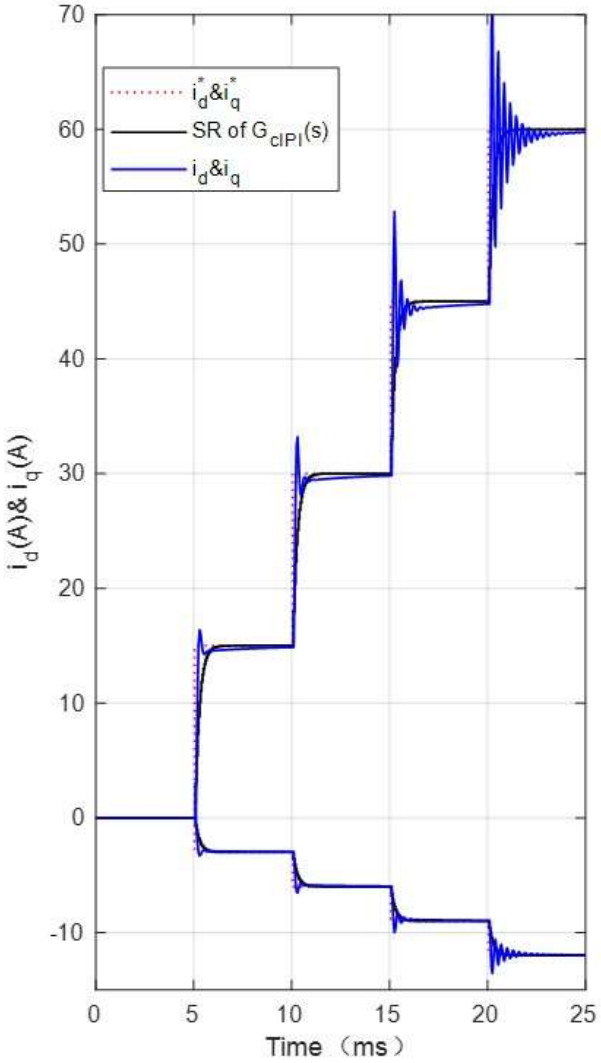

Figure 8. Simulation result of PI controller based on DIMC ($\alpha = 4000\text{rad/s}$) of the locked saturated machine.

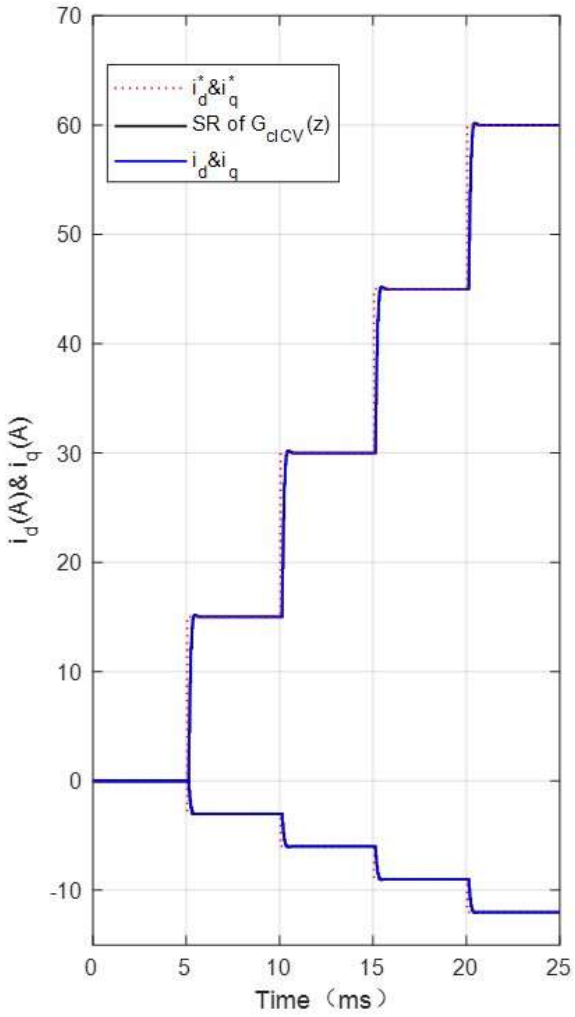

Figure 9. Simulation result of complex vector controller based on flux-linkage data ($k=0.3$) of the locked saturated machine.

3.3.2. Simulation of the High-Speed Machine

In the high-speed mode, the speed is set as 5000 rpm, which means that the fundamental frequency of the output current f_{out} is 833 Hz. The current reference value is less than the rated value. In order to improve the ratio of current frequency to sampling frequency, SSSU is adopted. The sampling frequency f_s is 10 kHz. The −3 dB bandwidth is set to 6473rad/s through making $\alpha=6473\text{rad/s}$, $k=0.3$.

Figures 10 and 11 present simulation results. The decoupled performance of the classical PI control system is unsatisfactory at high speed with rated current working conditions. This is because of the mismatch of inductance parameters and time delay. Furthermore, complex vector control, which is deducted from the accurate model, achieves perfect decoupling. The current trajectory follows the step response of the closed-loop transfer function $G_{clCV}(z)$ satisfactorily.

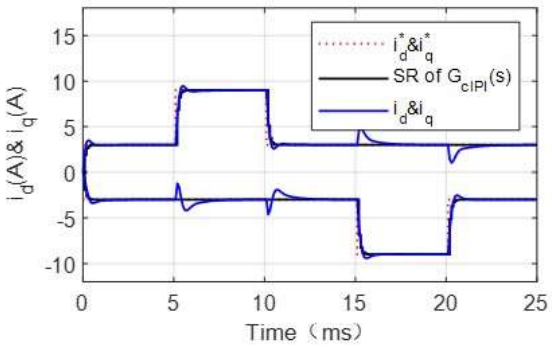

Figure 10. Simulation result of PI controller based on DIMC ($\alpha = 6473\text{rad/s}$, $f_s = 10\text{kHz}$) of the high-speed machine ($f_{out} = 833\text{Hz}$).

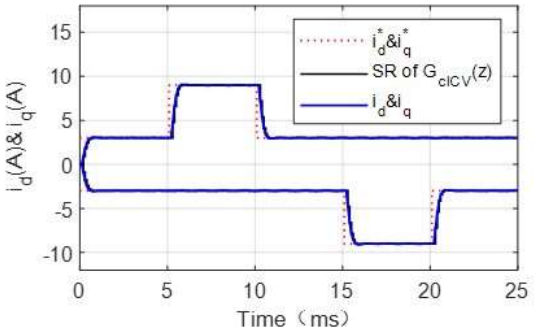

Figure 11. Simulation result of complex vector controller based on flux-linkage data ($k = 0.3$, $f_s = 10\text{kHz}$) of the high-speed machine ($f_{out} = 833\text{Hz}$).

3.3.3. Simulation of the High-Speed Saturated Machine

Now, set the speed to 5000 rpm and the sampling frequency to 10 kHz in the simulation. The parameters of both controllers are still the same, namely $\alpha = 6473\text{rad/s}$, $k = 0.3$. The quadrature axis current is given an incremental increase of 15 A each 5 ms from 0 to 60 A, while the direct axis current is given a decrease step of 3 A each 5 ms from 0 to −12 A.

The simulation results can be seen in Figures 12 and 13. For complex vector control, the current still agrees with the expected response and achieves good performance in the dynamic and steady state. In contrast, the classic PI control based on the DIMC principle fails to follow the instructions, especially in highly saturated situations.

The simulation results illustrate that the complex vector controller based on flux-linkage data is suitable for saturated and high-speed machines.

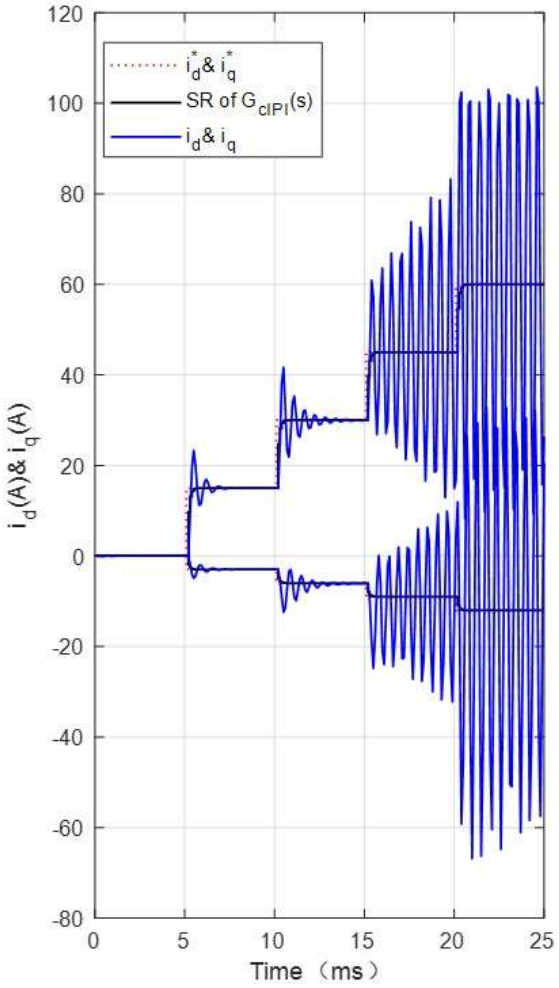

Figure 12. Simulation result of PI controller based on DIMC ($\alpha = 6473\text{rad/s}$, $f_s = 10\text{kHz}$) of the high-speed saturated machine ($f_{out} = 833\text{Hz}$).

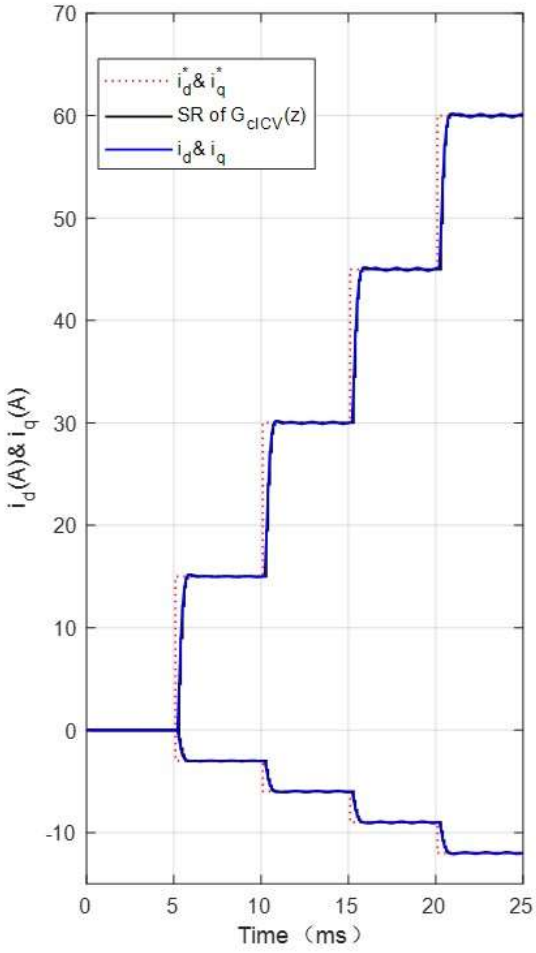

Figure 13. Simulation result of complex vector controller based on flux-linkage data ($k=0.3$, $f_s = 10\text{kHz}$) of the high-speed saturated machine ($f_{out} = 833\text{Hz}$).

4. Experiments

In this section, the experimental platform is introduced first. Then, the experiment results are presented.

4.1. Experiment Platform

Figure 14 presents the experiment platform. The motor under test (MUT) and load motor are installed on the bench. These two motors are powered by two VSIs. The data are sent to computers through USB-CAN interfaces. The data in DSP reflect the actual values of current loop controller; thus, the digital values transported to computer are used in the analysis of this study rather than analog value measured by current clamp [27]. The user interfaces on the computers can display data and send instructions. The magnetic particle brake is installed on the bench to lock the MUT when the parameters are measured, the inverter nonlinearity is measured, and the 0-speed current control performance experiment is carried out. Parameters of motor under test and load motor are shown in Table 1.

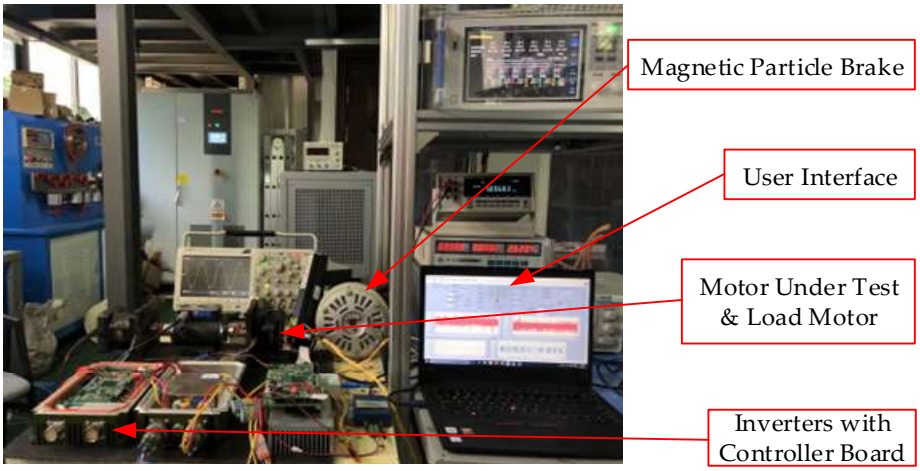

Figure 14. Experiment platform.

Table 1. Parameters of motor under test and load motor.

Parameters	Motor Under Test	Load Motor
Number of pole pairs	10	10
Stator winding resistance	0.8 Ω	1.5 Ω
d-axis inductance	0.69 mH [1]	0.63 mH [1]
q-axis inductance	0.74 mH [1]	0.67 mH [1]
PM flux-linkage	0.02 Wb	0.018 Wb
Rated speed	2000 rpm	2000 rpm
Maximum speed	5000 rpm	5000 rpm

[1] The data are measured at $i_d = -1.8\text{A}$, $i_q = 9\text{A}$.

The TMS320F28335 of Texas Instruments is adopted in the full-bridge inverter, which is made of IGBTs. The switching frequency of the inverter is 10 kHz. By using SSSU/DSDU, the sampling frequency is 10 kHz/20 kHz. DMA (Direct Memory Access) technology is used to increase the current sample accuracy. The look-up tables for $\psi_d\left(i_d, i_q\right)$ and $\psi_q\left(i_d, i_q\right)$ are saved in a flash. At the beginning of the program, the table is moved to RAM. The sine and cosine values are also computed after reset to increase code execution speed. The deadtime compensation algorithm is adopted to improve the accuracy of output voltage [28].

The parameters used in the PI controller are static inductance at $i_d = -1.8\text{A}$, $i_q = 9\text{A}$. As for the complex vector controller, calculating i_d and i_q, looking up to the table, and interpolation are implemented to get the value of $\psi_d\left(i_d, i_q\right)$ and $\psi_q\left(i_d, i_q\right)$. Instead of using current, flux linkage feedback can avoid the influence of the cross-saturation terms $l_{dq}\left(i_d, i_q\right) \cdot \mathrm{d}i_q/\mathrm{d}t$ and $l_{qd}\left(i_d, i_q\right) \cdot \mathrm{d}i_d/\mathrm{d}t$, which improves the performance of the current control.

The control software cannot show every sampling value in real time due to the capacity of the serial controller area network (CAN) bus communications. The sampled values are recorded in RAM every sampling period at running conditions. When the system stops, the recorded values are transmitted to the computer.

4.2. Experiment Results

4.2.1. Experiment Result of the Locked Saturated Machine

Lock the rotor through magnetic particle brake and set the control parameter/sampling frequency the same as simulation. The quadrature axis current is given with an incremental increase of 15 A from 0 to 60 A, 5 ms each. The direct axis current is given with a decrease step of 3 A from 0 to −12 A, 5 ms each.

The experiment results are consistent with the simulation results. For the classical PI controller, the current ringing effect becomes more and more distinct with the increasing current, as shown in Figure 15. At around 21 ms, the software protection is triggered. The result represents that the dynamic and steady-state performance of the PI controller based on IMC is not guaranteed when the iron core is saturated. Although the current i_d demagnetizes the magnetic circuit in this experiment, the cross saturation reduces the direct-axis inductance. Figure 16 will be discussed in Section 4.2.3. for coherence. Figure 17 presents the experiment result of complex vector control. The response of each step is presented separately to show the detailed results. The current response follows the step response of the closed-loop transfer function satisfactorily. The usage of flux-linkage data can compensate for the parameter mismatch of inductance.

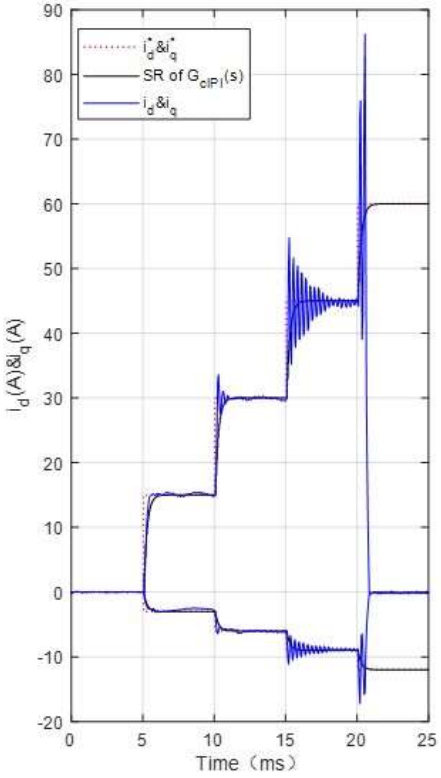

Figure 15. Experiment result of PI controller based on DIMC ($\alpha = 4000\text{rad/s}$) of the locked saturated machine.

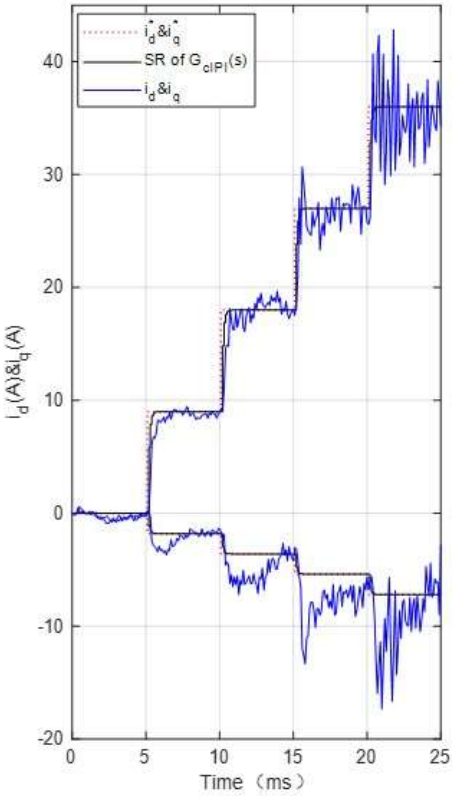

Figure 16. Experiment result of PI controller based on DIMC ($\alpha = 6473\text{rad/s}$, $f_s = 10\text{kHz}$) of the high-speed saturated machine ($f_{out} = 833\text{Hz}$).

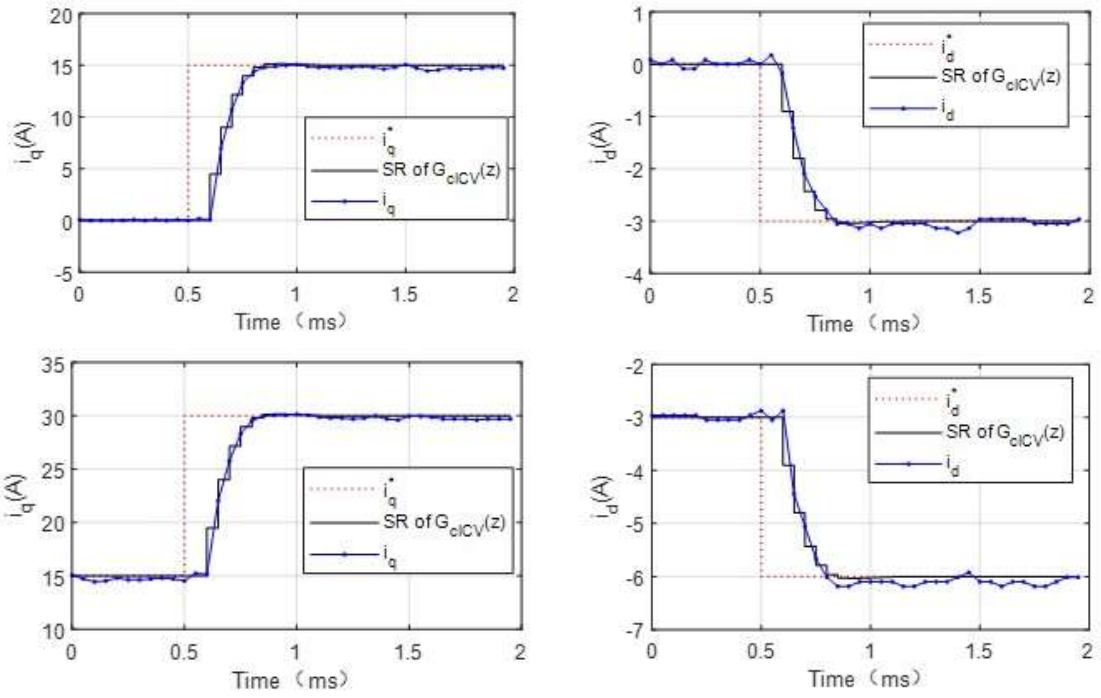

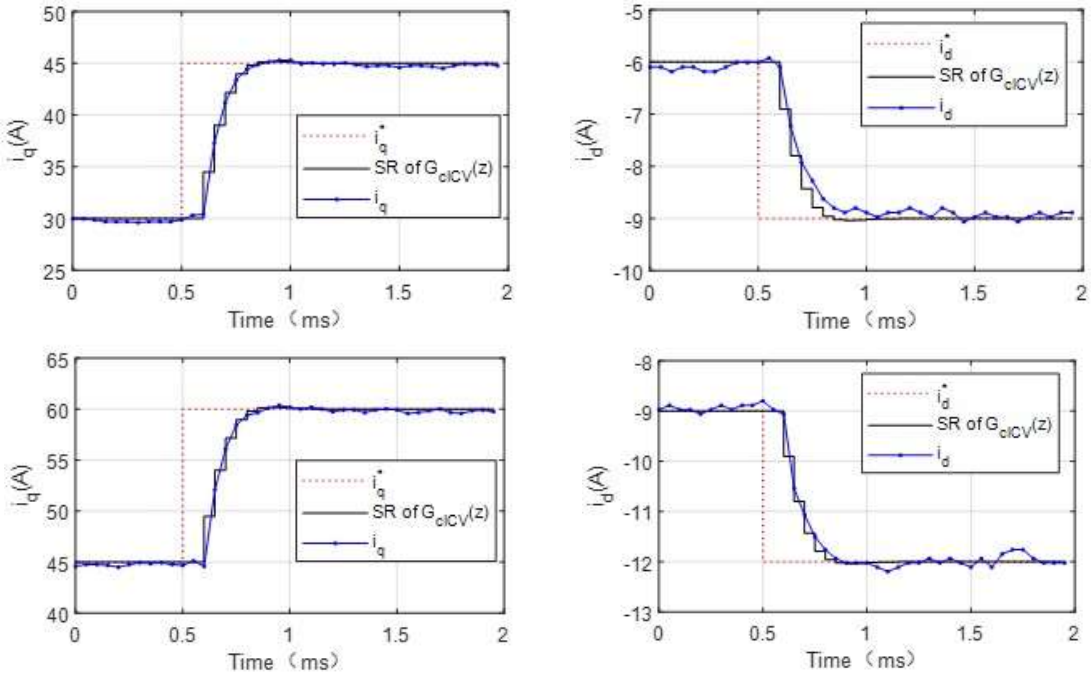

Figure 17. Experiment result of complex vector controller based on flux-linkage data ($k=0.3$) of the locked saturated machine.

4.2.2. Experiment Result of the High-Speed Machine

The load motor is used to control the speed at 5000 rpm. The dq axis of the motor is given with pulse reference currents in turn which are not greater than the rated current, and the step response and decoupling performance are observed. Controller parameters and sampling time are the same as the simulation values.

Figures 18–20 present the experiment results, consistent with the simulation results. The steady and dynamic performance of the complex vector controller is better than that of the classical PI controller at $f_{out}=833\text{Hz}$. With the proposed controller, the current oscillation caused by coupling effect decreases from 1.8 to 0.6 A. The almost perfect decoupling performance in high-speed working conditions is achieved by using the complex vector controller. By putting the *d*-*q* current into the X–Y plot, the fluctuation of complex vector controller steady current at (−3 A, 9 A), (−9 A, 3 A), (−3 A, 3 A) is gentler than that of the PI controller. At the time of 5.5, 10.5, 15.8, and 20.5 ms, it can be seen that the deviation between the current under PI control and the reference current is more significant than that under the complex vector controller.

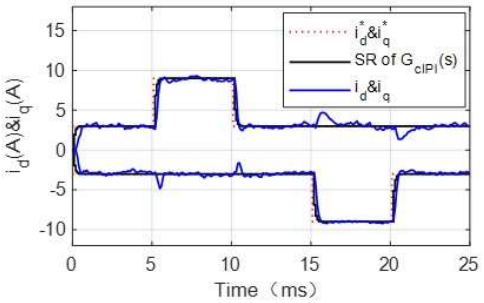

Figure 18. Experiment result of PI controller based on DIMC ($\alpha=6473\text{rad/s}$, $f_s=10\text{kHz}$) of the high-speed machine ($f_{out}=833\text{Hz}$).

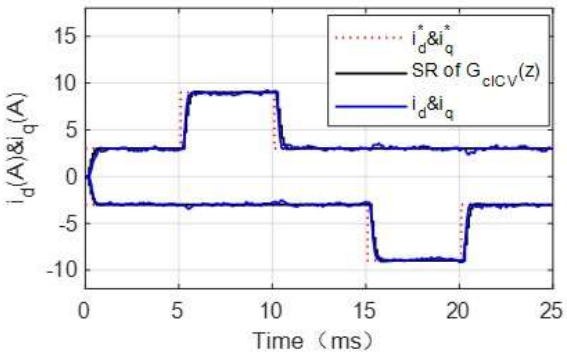

Figure 19. Experiment result of complex vector controller based on flux-linkage data ($k=0.3$, $f_s=10\text{kHz}$) of the high-speed machine ($f_{out}=833\text{Hz}$).

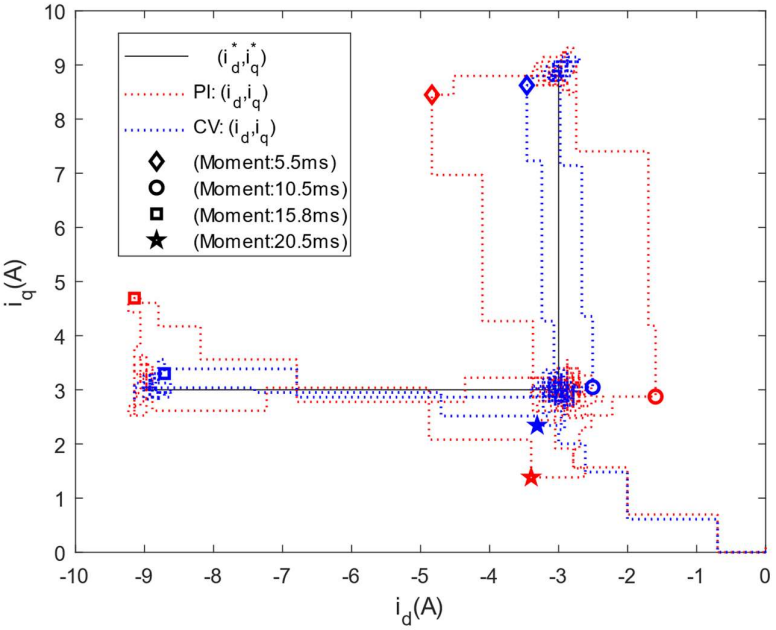

Figure 20. X-Y graph of the *d-q* current under PI controller based on DIMC ($\alpha=6473\text{rad/s}$, $f_s=10\text{kHz}$) and complex vector controller based on flux-linkage data ($k=0.3$, $f_s=10\text{kHz}$) of the high-speed machine ($f_{out}=833\text{Hz}$).

4.2.3. Experiment Result of the High-Speed Saturated Machine

The load motor is used to control the speed at 5000 rpm. Controller parameters and sampling time are the same as the simulation values. During the verification of the PI controller, the quadrature axis current is given with an incremental increase of 9 A from 0 to 36 A, 5 ms each, to prevent the current loop from collapsing. The quadrature axis current is given with an incremental increase of 15 A from 0 to 60 A, 5 ms each, which is the same as simulation. Both reference values of the direct axis current are set as $i_d^*=-0.2*i_q^*$.

The experiment results of both controllers under saturated high-speed working conditions are presented in Figures 16 and 21. At high speed, the control performance of the classical PI controller deteriorates with the increasing saturation. The response of each step is shown separately to describe the detailed results. With the proposed controller, the peak quadrature axis current is improved from 36 to 60 A, and the peak direct axis current

is improved from 7.2 to 12 A, which improves the output power by 39%. At the fundamental frequency of output current, which is 833 Hz, the current response follows the step response of the closed-loop transfer function satisfactorily. The increase in the current ripple is inevitable because of the decrease in the inductance.

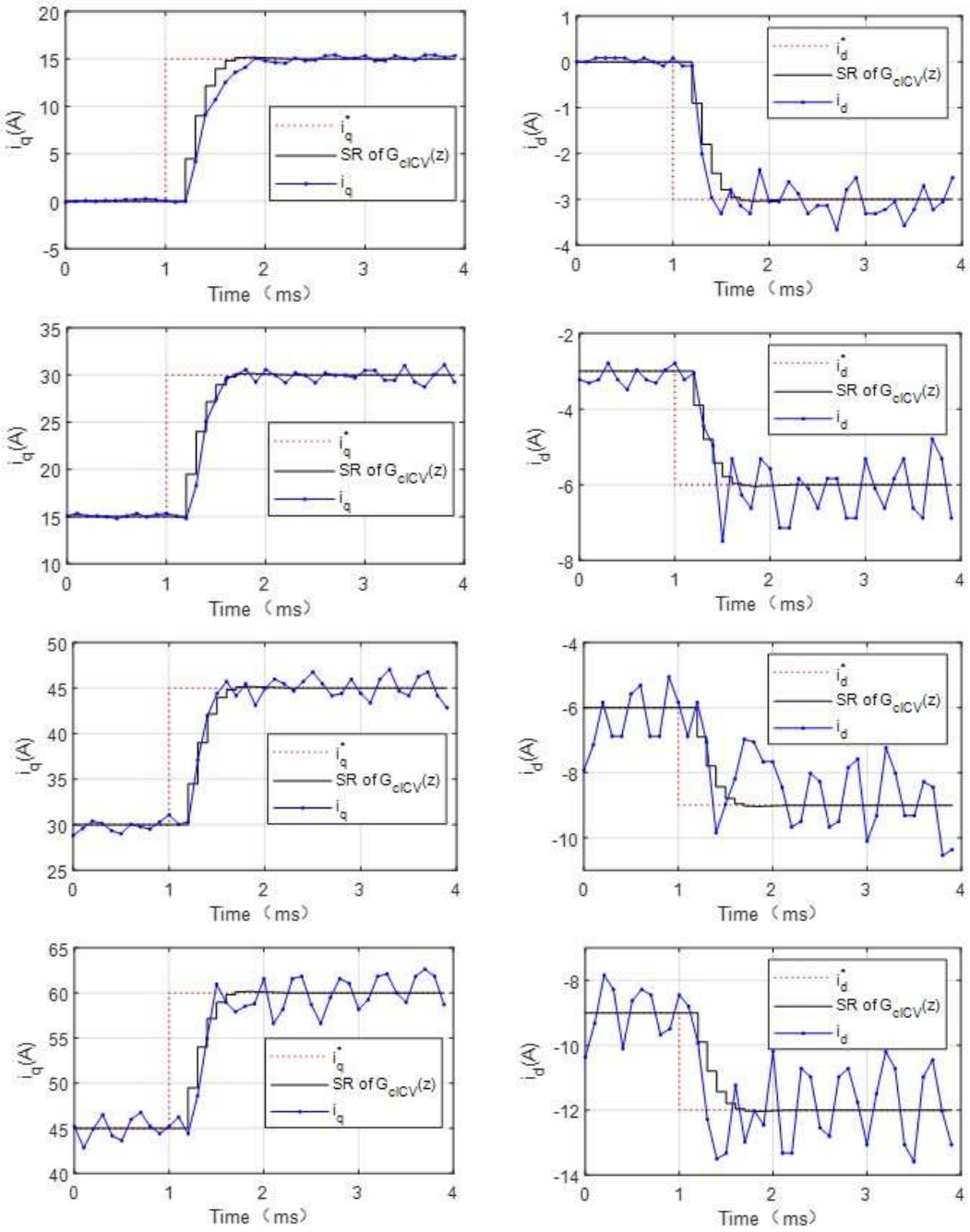

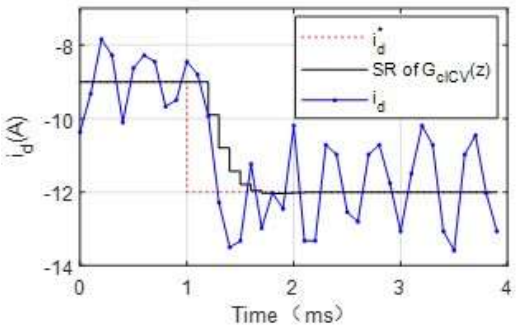

Figure 21. Experiment result of complex vector controller based on flux-linkage data ($k=0.3$, $f_s = 10\text{kHz}$) of the high-speed saturated machine ($f_{out} = 833\text{Hz}$).

5. Conclusions

In this research, the accurate PMSM model with cross saturation is introduced. The influence of time delay in the digital control system is analyzed. The flux-linkage values at different current conditions are measured. Then, a controller based on the flux data is proposed to mitigate the delay and parameters mismatch problems. To verify the performance, simulation and experiment of PI control based on DIMC principle and complex vector control based on the flux-linkage data are carried out. As a comparative case, the performance of the PI controller based on DIMC matches the desired bandwidth target in unsaturated circumstances. The proposed controller achieves better bandwidth and decoupled performance than the DIMC PI controller. It can improve the peak current output region at high speed, which can improve the maximum output power by 39%. However, the parameters are prone to be affected by temperature, which is not included in this research. The nonlinearity caused by temperature will be investigated in future work.

Author Contributions: Conceptualization, H.M., L.L. and Y.F.; data curation, H.M. and Z.J.; formal analysis, H.M.; methodology, H.M., L.L., Y.F. and Y.G.; project administration, J.L.; resources, Z.J. and J.L.; software, H.M.; supervision, L.L., Y.G. and J.L.; validation, Z.J.; visualization, H.M.; writing—original draft, H.M.; writing—review & editing, L.L., Y.G. and J.L. All authors have read and agreed to the published version of the manuscript.

Funding: This research was funded by the Technology Developing Foundation of Pudong New District under Grant PKX2020-R08.

Institutional Review Board Statement: Not applicable.

Informed Consent Statement: Not applicable.

Data Availability Statement: Not applicable.

Conflicts of Interest: The authors declare no conflict of interest.

References

1. Hoffmann, N.; Fuchs, F.W.; Kazmierkowski, M.P.; Schröder, D. Digital current control in a rotating reference frame-Part I: System modeling and the discrete time-domain current controller with improved decoupling capabilities. *IEEE Trans. Power Electron.* **2015**, *31*, 5290–5305.
2. Weihua, W.; Xi, X. An improved pi regulator for current loop of PMSM taking one-step-delay into consideration. *Proc. CSEE* **2014**, *34*, 1882–1888.
3. Guo, J.; Fan, T.; Li, Q.; Wen, X. Coupling and Digital Control Delays Affected Stability Analysis of Permanent Magnet Synchronous Motor Current Loop Control. In Proceedings of the 2019 IEEE Vehicle Power and Propulsion Conference (VPPC), Hanoi, Vietnam, 14–17 October 2019; IEEE: New York, NY, USA, 2019.
4. Rovere, L.; Formentini, A.; Zanchetta, P. FPGA implementation of a novel oversampling deadbeat controller for PMSM drives. *IEEE Trans. Ind. Electron.* **2018**, *66*, 3731–3741.
5. Young, H.A.; Perez, M.A.; Rodriguez, J. Analysis of finite-control-set model predictive current control with model parameter mismatch in a three-phase inverter. *IEEE Trans. Ind. Electron.* **2016**, *63*, 3100–3107.

6. Gonçalves, P.; Cruz, S.; Mendes, A. Finite control set model predictive control of six-phase asymmetrical machines—An overview. *Energies* **2019**, *12*, 4693.
7. Yang, S.Y.; Wang, Y.Z.; Chu, Z.H.; Xie, Z. Current decoupling control of PMSM based on an extended state observer with continuous gains. *Proc. CSEE* **2020**, *40*, 1985–1997.
8. Kiyota, K.; Kakishima, T.; Sugimoto, H.; Chiba, A. Comparison of the test result and 3D-FEM analysis at the knee point of a 60 kW SRM for a HEV. *IEEE Trans. Magn.* **2013**, *49*, 2291–2294.
9. Astrom, K.J. Adaptive control around 1960. *IEEE Control. Syst. Mag.* **1996**, *16*, 44–49.
10. Jung, J.W.; Leu, V.Q.; Do, T.D.; Kim, E.K.; Choi, H.H. Adaptive PID speed control design for permanent magnet synchronous motor drives. *IEEE Trans. Power Electron.* **2014**, *30*, 900–908.
11. Jung, J.W.; Choi, Y.S.; Leu, V.Q.; Choi, H.H. Fuzzy PI-type current controllers for permanent magnet synchronous motors. *IET Electr. Power Appl.* **2011**, *5*, 143–152.
12. Chang, S.H.; Chen, P.Y.; Ting, Y.H.; Hung, S.W. Robust current control-based sliding mode control with simple uncertainties estimation in permanent magnet synchronous motor drive systems. *IET Electr. Power Appl.* **2010**, *4*, 441–450.
13. Li, Z.; Wang, F.; Ke, D.; Li, J.; Zhang, W. Robust continuous model predictive speed and current control for PMSM with adaptive integral sliding-mode approach. *IEEE Trans. Power Electron.* **2021**, *36*, 14398–14408.
14. Xia, C.; Yan, Y.; Song, P.; Shi, T. Voltage disturbance rejection for matrix converter-based PMSM drive system using internal model control. *IEEE Trans. Ind. Electron.* **2011**, *59*, 361–372.
15. Fu, X.; He, H.; Xu, Y.; Fu, X. A Strongly Robust and Easy-Tuned Current Controller for PMSM Considering Parameters Variation. *IEEE Access* **2020**, *8*, 44228–44238.
16. Economou, C.G.; Morari, M.; Palsson, B.O. Internal model control: Extension to nonlinear system. *Ind. Eng. Chem. Process Des. Dev.* **1986**, *25*, 403–411.
17. Zhong, Z.F.; Jin, M.J.; Shen, J.X. Full speed range sensorless control of permanent magnet synchronous motor with phased PI regulator-based model reference adaptive system. *Proc. CSEE* **2018**, *38*, 1203–1211.
18. Novotny, D.W.; Lipo, T.A. *Vector Control and Dynamics of AC Drives*; Oxford University Press: New York, NY, USA, 1996.
19. Yuan, X.; Chen, J.; Jiang, C.; Lee, C.H. Discrete-time current regulator for AC machine drives. *IEEE Trans. Power Electron.* **2021**, *37*, 5847–5858.
20. Awan HA, A.; Saarakkala, S.E.; Hinkkanen, M. Flux-linkage-based current control of saturated synchronous motors. *IEEE Trans. Ind. Appl.* **2019**, *55*, 4762–4769.
21. Kim, H.; Degner, M.W.; Guerrero, J.M.; Briz, F.; Lorenz, R.D. Discrete-time current regulator design for AC machine drives. *IEEE Trans. Ind. Appl.* **2010**, *46*, 1425–1435.
22. Rallabandi, V.; Taran, N.; Ionel, D.M.; Zhou, P. Inductance testing for IPM synchronous machines according to the new IEEE Std 1812 and typical laboratory practices. *IEEE Trans. Ind. Appl.* **2019**, *55*, 2649–2659.
23. Wang, Q.; Wang, G.; Zhao, N.; Zhang, G.; Cui, Q.; Xu, D. An Impedance Model-Based Multiparameter Identification Method of PMSM for Both Offline and Online Conditions. *IEEE Trans. Power Electron.* **2021**, *36*, 727–738.
24. Chen, X.; Wang, J.; Sen, B.; Lazari, P.; Sun, T. A high-fidelity and computationally efficient model for interior permanent-magnet machines considering the magnetic saturation, spatial harmonics, and iron loss effect. *IEEE Trans. Ind. Electron.* **2015**, *62*, 4044–4055.
25. Harnefors, L.; Nee, H.P. Model-based current control of AC machines using the internal model control method. *IEEE Trans. Ind. Appl.* **1998**, *34*, 133–141.
26. Luo, G.; Zhang, R.; Chen, Z.; Tu, W.; Zhang, S.; Kennel, R. A novel nonlinear modeling method for permanent-magnet synchronous motors. *IEEE Trans. Ind. Electron.* **2016**, *63*, 6490–6498.
27. Yang, S.; Wang, Q.; Xie, Z.; Zhang, X.; Chang, L. Digital current controller with a novel active damping design for IPMSM. *IEEE Trans. Energy Convers.* **2021**, *37*, 185–197.
28. Dead-Time Compensation Method for Vector-Controlled VSI Drives Based on Qorivva Family. Available online: https://www.nxp.com/docs/en/application-note/AN4863.pdf (accessed on 16 March 2022).